HHS Public Access

Author manuscript

Nat Phys. Author manuscript; available in PMC 2016 October 25.

Published in final edited form as:

Nat Phys. 2016 ; 12: 830–834. doi:10.1038/nphys3734.

A Universal Moiré Effect and Application in X-Ray Phase-Contrast Imaging

Houxun Miao[1], **Alireza Panna**[1], **Andrew A. Gomella**[2], **Eric E. Bennett**[1], **Sami Znati**[1], **Lei Chen**[3], and **Han Wen**[1]

[1]Biophysics and Biochemistry Center, National Heart, Lung and Blood Institute, National Institutes of Health, Bethesda, Maryland, USA

[2]Sidney Kimmel Medical College, Thomas Jefferson University, Philadelphia, Pennsylvania, USA

[3]Center for Nanoscale Science and Technology, National Institute of Standards and Technology, Gaithersburg, Maryland, USA

Abstract

A moiré pattern is created by superimposing two black-and-white or gray-scale patterns of regular geometry, such as two sets of evenly spaced lines. We observed an analogous effect between two transparent phase masks in a light beam which occurs at a distance. This phase moiré effect and the classic moiré effect are shown to be the two ends of a continuous spectrum. The phase moiré effect allows the detection of sub-resolution intensity or phase patterns with a transparent screen. When applied to x-ray imaging, it enables a polychromatic far-field interferometer (PFI) without absorption gratings. X-ray interferometry can non-invasively detect refractive index variations inside an object[1–10]. Current bench-top interferometers operate in the near field with limitations in sensitivity and x-ray dose efficiency[2, 5, 7–10]. The universal moiré effect helps overcome these limitations and obviates the need to make hard x-ray absorption gratings of sub-micron periods.

The classic moiré effect is the product of two intensity patterns of slightly different sizes or orientations. It can be found in a variety of forms in diverse applications including metrology, precision measurements, alignment and imaging[11–13]. Transparent phase masks, or phase gratings, imprint a periodic phase pattern on a wave front. When two such gratings are overlaid in a light beam, there is no moiré effect immediately behind the gratings in the near field; we did, however, observe an achromatic intensity pattern in the far field. Its spatial frequency equals the difference between the projected frequencies of the two

Correspondence and requests for materials should be addressed to H.W. (wenh@nhlbi.nih.gov) or H.M. (miaoh@mail.nih.gov).

Author contributions

H.M., A.P. and H.W. performed the experiments. H.M., L.C. and S.Z. performed fabrication. A.A.G., A.P., E.E.B., H.M. and H.W. built the systems. H.W. and H.M. performed the theoretical modeling and numerical calculations. H.W. and H.M. wrote the manuscript with input from all authors.

Competing financial interests

The authors declare no competing financial interests.

Additional information

Two supplementary figures and three supplemental videos are included in the manuscript.

gratings. The two gratings can either be in contact or have a finite spacing. We show that this phase moiré effect and the classic effect are the extremes of a general effect for masks that mix phase and amplitude modulations to various degrees.

In the experiment illustrated in Fig. 1a, two identical visible-light phase gratings of the same 14.3 μm period (G_1 and G_2) were overlaid in parallel planes. They were illuminated by a white-light cone beam from a source of 0.44 mm size and projected onto a frosted-glass image screen (See supplemental Fig. 1 for a photo of the setup, the light spectrum and the phase-shift profile of the gratings). The geometric distances were L_1=18.0 cm from the source to the first grating, L_2 varying between 5 mm and 20.5 cm from the 2nd grating to the image screen, and the inter-grating spacing D fixed at 0.41 mm. Broad intensity fringes emerged as the image screen moved away from the gratings (Fig. 1b). Supplemental video 1 shows the full images when scanning the position of the image screen.

An intuitive explanation of the phase moiré effect is illustrated in Fig. 1c. The cone beam projects the self-images of G_1 onto the plane of G_2 with a slightly magnified period P_1[14], resulting approximately in a combined phase oscillation of the form $\phi[\cos(2\pi x/P_1)+\cos(2\pi x/P_2)]$, where P_2 is the period of G_2. It can be written as $2\phi\cos[\pi x(1/P_1-1/P_2)]\cos[\pi x(1/P_1+1/P_2)]$, which is equivalent to a single phase grating whose phase shift is modulated by a beat pattern. The beat pattern represents alternating strongly and weakly diffracting areas. Light that transmits through the strongly diffracting areas are diverted into side diffraction orders and away from the direction of straight radial projection. After a sufficient distance, the re-direction of the flux gives rise to periodic intensity fringes as shown in Fig. 1c. The measured and theoretical dependence of the fringe visibility on the position of the image screen are summarized in Fig. 1d. Fringe visibility is fringe amplitude/mean intensity, or $(I_{max}-I_{min})/(I_{max}+I_{min})$.

The moiré carpet in Fig. 2a experimentally shows the progression of the moiré fringes with the inter-grating spacing D in the range between 0.05 mm and 5 mm. The image screen was fixed at 20 cm from the source. The gratings were placed mid-way between them. As D increases, the difference in the projected frequencies of the gratings also increases, leading to denser fringes. Coherent interference between different diffraction orders occurs in the space between the gratings and produces the appropriate self-images of G_1 at the G_2 plane at regular intervals[14] of D. Therefore, the fringe contrast underwent a periodic oscillation and gradually diminished with increasing D due to the broad spectrum of the light. The interval of oscillation is theoretically[14] $2P^2/\lambda$. The measured value of 0.74±0.09 mm matches the 550 nm average wavelength of the white light spectrum (Supplemental Fig. 1). The measured and theoretically calculated fringe visibilities as a function of the spacing D are shown in Fig. 2b. The measured fringe spatial frequency as a function of D is also predictable by theory (Fig. 2b). Supplemental video 2 shows the full images when scanning D.

Theoretical derivation of the general situation of a polychromatic cone-beam illuminating a pair of gratings of different periods is provided in the Methods section. The phase moiré effect and the classic moiré effect are at the two extremes. With pure amplitude gratings the classic moiré effect appears immediately behind the gratings. There is no requirement on the

lateral coherence of the light source. With pure phase gratings the phase moiré effect appears at a distance from the gratings; the lateral coherence of the light at the first grating should be about the period of the grating. A continuous transition exists between the two extremes for any combination of intensity and phase modulations.

For phase-contrast imaging applications that require high sensitivity, the space between the gratings can be the preferred location to place the objects, since coherent wave interference occurs here. With this in mind, a three-grating setup (Fig. 3a) has the advantage that it allows the gratings to be widely separated. Here, the G2 grating refocuses the diffracted waves from G_1 into a series of achromatic Fourier images at a specific plane downstream[14]. The G_3 grating is placed on or near this plane to produce moiré effects between itself and the Fourier images. See Methods section for the theoretical formulas of the three-grating setup. Similar to the two-grating system, the G_1 grating can be a pure intensity or a pure phase grating as the two extreme cases. The former allows an extended light source with minimal lateral coherence but at the cost of light reduction by G_1; the latter requires the lateral coherence of the source at G_1 to be about the grating period.

The phase moiré effect is now recognized as the underlying mechanism of a type of x-ray interferometer that uses only phase gratings, which has previously demonstrated an order of magnitude increase in sensitivity and reduction in radiation dose when compared with the current Talbot-Lau interferometer[15]. This understanding leads to the use of purposely mismatched grating periods to substantially improve the efficiency of the x-ray PFI. The improved design has three phase gratings of 1 mm by 7 cm area and periods of 399 nm, 400 nm and 400 nm, respectively. Grating fabrication is described in ref. [16]. The x-ray tube had a rhenium-tungsten anode and operated at 40kVp/40mA. A 70 μm-wide slit was placed on the x-ray tube window to limit the vertical size of the source while keeping sufficient angular spread of the beam to cover the grating area. See Supplemental Fig. 2 for a photo of the system. The geometric distances illustrated in Fig. 3a were L_1=0.391 m, D_1=0.463 m, L_3=0.710 m. The distance D_3 was scanned over the range of D_1 +/− 8 mm. The cross-section profiles of the gratings (Fig. 3b) were obtained with scanning electron microscopy (SEM). The gratings are designed for phase shifting but also contain material absorption. From these profiles both the phase shift and linear attenuation profiles were extracted for photon energies of 20 to 40 keV (data at 27.5 keV are plotted in Fig. 3c). The G_2 profile was designed to maximize light diffraction into the ±1 orders.

The moiré carpet in Fig. 4a shows the evolution of the moiré fringes with the changing G_3 position. Full-field images were provided in Supplemental video 3. The measured and theoretically calculated fringe visibility and frequency curves are shown in Fig. 4b for the case of parallel grating planes. The fringe visibility increased with out-of-plane tilting of the gratings. With G_3 positioned at $D_3 - D_1 = 1.2$ mm, the measured and theoretically calculated fringe visibility curves as functions of the tilt angles of G_1 and G_3 are shown in Figures 4c and 4d, respectively. The out-of-plane tilt mainly altered the transmission profiles of the gratings. Their influence on the fringe contrast is discussed in the Methods section. The peak fringe visibility of 19.4% was attained when both G_1 and G_3 were tilted at 1.2°. This is a 43% increase in fringe visibility over the previous 13.5% value[15] due to the use of mismatched grating periods.

In imaging experiments the samples are positioned behind grating G_2 (Fig. 3a) where vertically separated light paths coherently interfere. A local gradient of the refractive index causes a phase shift of the moiré fringes. An image of the phase shift is a differential phase image. A second measurement is the attenuation of the fringe amplitude due to perturbations by the object that reduce the mutual coherence of the light paths. This provides a de-coherence image. The raw projection images were taken in a phase-stepping procedure[7, 8, 17] and processed with an adaptive algorithm to deal with mechanical fluctuations. A complete data set included 10 images of 1 second exposure each, at a total entrance surface radiation dose (ESD) of 0.71 mGy. The grating area determined a 0.7 mm by 5 cm field of view at the sample. Samples were scanned at 0.7 mm steps and multiple fields of view were tiled to cover the desired height.

Figure 5a shows a reference image without any sample. It appears stretched in the vertical direction due to an oblique incident angle of 4.5° of the beam on the detector screen for improved efficiency and vertical resolution[18]. The grating G_3 was slightly rotated around the beam axis to cause the inclination of the fringes from being horizontal. Figures 5b–5d are multimodal projection images of a formalin-fixed, unstained mouse kidney specimen immersed in water, including the differential phase, de-coherence and conventional attenuation-contrast radiography. Although a single projection, the outline and internal blood vessels of the kidney become visible in the differential phase image (Fig. 5b). The accompanying de-coherence image (Fig. 5c) shows reduced coherence in the peripheral fat tissue (white arrows) and also in areas containing steep gradients of the differential phase, such as the bright edges of the graduation marks on the centrifuge tube. This is caused by a large dispersion of the fringe phase within a pixel[19]. The conventional radiography (Fig. 5d) was taken with a flat-panel x-ray detector at a dose of 4.47 mGy ESD. A photograph of the specimen is shown in Fig. 5e.

Generally when creating a distant moiré pattern with a phase grating, the fringe period scales inversely with the grating period (see Eq. 17 in Methods). Therefore, smaller grating periods allow shorter observation distances. In ideal situations the moiré fringe visibility between two phase gratings and among three phase gratings are estimated at 81% and 33%, respectively. Practically the visibility is reduced by less than ideal grating profiles, scattering in the grating material, spectral dispersion of the grating phase shift with a broad-band source and the detector resolution.

While the self-imaging of gratings is a coherent interference effect[20], the universal moiré effect is at its core an incoherent intensity effect. With highly coherent sources such as a point monochromatic source, the self or Fourier images of gratings may coexist with the moiré effect in the form of fine fringes super-imposed on broad moiré patterns. The moiré effect between phase masks still requires a certain level of lateral coherence of the illumination, since the effect appears at a standoff distance from the masks. It is shown in Methods that the lateral coherence length of the illumination at the first phase grating should be comparable to the grating period. One the other hand, a first amplitude grating segments the incident beam and removes the coherence requirement on the illumination similar to the Lau effect, which is detailed in Methods.

Due to its simplicity and robustness towards environmental factors, the phase moiré effect was recently implemented for polychromatic and monochromatic cold neutron sources in quantum information and imaging research using pure silicon gratings as phase masks[21]. In a broad sense the universal moiré effect occurs when a periodic screen is placed on a periodically modulated wave front. The periodic wave front can be the Fourier image of other grating(s) upstream. The classic moiré effect is a special case where the screen is an intensity mask. Our finding shows that one can use a phase mask as the screen. The effect also occurs for pure phase modulations which are not visible by direct observation of the intensity distribution.

Methods

Theoretical modeling of the universal moiré effect between two diffraction gratings

The theory applies to the general case of a cone-beam illuminating a pair of diffraction gratings of different periods with a possible spacing between them. The gratings can modulate the phase or amplitude or both of the beam. Two assumptions are made: the wavelength $\lambda \ll$ grating periods; the gratings act as multiplicative transmission functions on the complex amplitude wave front. The moiré effect is shown to be determined by auto-correlation functions of the grating transmission profiles.

Referring to the schematics of Fig. 1a, the scalar field at a point y on the image plane is given by the Fresnel-Kirchhoff integral of diffraction[20]

$$V(y) \propto \iint \frac{1}{r_0 r_1 r_2} \exp[ik(r_0+r_1+r_2)] T_1(y_1) T_2(y_2) dy_1 dy_2, \quad (1)$$

where k is the wave number in vacuum, y_1 and y_2 are coordinates in the G_1 and G_2 planes; r_0, r_1 and r_2 are the successive spacinggs between the source, the points y_1, y_2 and y, respectively; T_1 and T_2 are the complex grating transmission functions. They are further written in Fourier series as

$$T_1(y_1) = \sum A_m \exp(i2\pi m f_1 y_1), \text{and} \quad (2)$$

$$T_2(y_2) = \sum B_n \exp(i2\pi n f_2 y_2), \quad (3)$$

where f_1 and f_2 are the spatial frequencies of the gratings. The vertical coordinate of the source is y_s. Substituting Eq. 2 and 3 into Eq. 1, expanding the phase factor of each $A_m B_n$ term to the second order around its minimum point at $\partial\phi/\partial y_f = 0$ and carrying through the Fresnel integral leads to an explicit expression of the wave field

$$V(y) \propto \exp(ik\,L/\cos\theta)\sum_{m,n} A_m B_n \exp[i\varnothing_0(m,n)+i\varnothing_1(m,n)], \quad (4)$$

where θ is the elevation angle of the line connecting the source to point y (Fig. 1a),

$$\varnothing_0(m,n)=2\pi m f_1\left(\frac{L_1}{L}y+\frac{D+L_2}{L}y_s\right)+2\pi n f_2\left(\frac{L_1+D}{L}y+\frac{L_2}{L}y_s\right), \quad (5)$$

and

$$\varnothing_1(m,n)=-\frac{L}{2k\cos^3\theta}\left[(2\pi m f_1)^2 L_1/L+(2\pi n f_2)^2 L_2/L-(2\pi m f_1 L_1/L-2\pi n f_2 L_2/L)^2\right]. \quad (6)$$

Considering the phase difference between the A_mB_n and the $A_{m+1}B_{n-1}$ terms, which contains an achromatic part

$$\varnothing_0(m,n)-\varnothing_0(m+1,n-1)=2\pi\left(f_2\frac{L_1+D}{L}-f_1\frac{L_1}{L}\right)y+2\pi\left(f_2\frac{L_2}{L}-f_1\frac{D+L_2}{L}\right)y_s, \quad (7)$$

and a wavelength-dependent part

$$\varnothing_1(m,n)-\varnothing_1(m+1,n-1)=2\pi\left(m+\frac{1}{2}\right)\delta_1(\lambda)-2\pi\left(n-\frac{1}{2}\right)\delta_2(\lambda), \quad (8)$$

where the increments are

$$\delta_1(\lambda)=\frac{\lambda}{L\cos^3\theta}f_1 L_1[(f_1-f_2)L_2+f_1 D], \quad (9)$$

and

$$\delta_2(\lambda)=\frac{\lambda}{L\cos^3\theta}f_2 L_2[(f_2-f_1)L_1+f_2 D], \quad (10)$$

The achromatic part (Eq. 7) implies the potential for a moiré pattern at the image plane with a wavelength-independent period of

$$P_d = L/[(f_2 - f_1)L_1 + f_2 D]. \quad (11)$$

The moiré fringes arise from the product of the $A_m B_n$ and $A_{m+1} B_{n-1}$ terms in the image intensity distribution of $|V(y)|^2$. Its complex amplitude according to Eq. 7 and 8 is

$$H_1(\lambda) \propto \exp[i(\frac{2\pi y}{P_d} - \frac{2\pi y_s}{P_s})] \sum_m A_m A_{m+1}^* e^{i2\pi(m+1/2)\delta_1} \sum_n B_n B_{n-1}^* e^{-i2\pi(n-1/2)\delta_2}. \quad (12)$$

Noting that the phase of the pattern also depends cyclically on the source position with a period of

$$P_s = L/[(f_1 - f_2)L_2 + f_1 D]. \quad (13)$$

this is called the source period. The summations in Eq. 12 are in fact Fourier coefficients of autocorrelation functions of the grating transmission profiles, known as the ambiguity function in waveform analysis:

$$\sum_m A_m A_{m+1}^* e^{i2\pi\left(m+\frac{1}{2}\right)\delta_1} = \chi_1(\delta_1 P_1, f_1) = \frac{1}{P_1} \int_0^{P_1} T_1(\xi + \delta_1 P_1/2) T_1^*(\xi - \delta_1 P_1/2) \exp(i2\pi\xi f_1) d\xi,$$

(14)

and

$$\sum_n B_n B_{n-1}^* e^{-i2\pi(n-1/2)\delta_2} = \chi_2^*(\delta_2 P_2, f_2) = \left[\frac{1}{P_2} \int_0^{P_2} T_2(\xi + \delta_2 P_2/2) T_2^*(\xi - \delta_2 P_2/2) \exp(i2\pi\xi f_2) d\xi \right]^*.$$

(15)

Substituting Eq. 14 and 15 into Eq. 12 provides a closed-form expression of the moiré fringe contrast. The Fourier coefficient of the fringe amplitude normalized to the mean intensity is

$$\frac{H_1(\lambda)}{H_0} = \frac{\chi_1(\delta_1 P_1, f_1)}{\langle T_1 T_1^* \rangle} \frac{\chi_2^*(\delta_2 P_2, f_2)}{\langle T_2 T_2^* \rangle}, \quad (16)$$

where $\langle T_j T_j^* \rangle$ denotes the average intensity transmission through a grating.

The fringe and source periods in Eq. 11 and 13 can be written in terms of the autocorrelation distances $\delta_f(\lambda)$ as

$$P_d = \frac{1}{\delta_2(\lambda)\cos^3\theta}\frac{\lambda}{P_2}L_2, \text{and} \quad (17)$$

$$P_s = \frac{1}{\delta_1(\lambda)\cos^3\theta}\frac{\lambda}{P_1}L_1. \quad (18)$$

Several physical facts of the universal moiré effect emerge from the formulas. For a polychromatic source, the fringe contrast is a weighted average of Eq. 16 over the light spectrum. The key determinant of the moiré effect is the auto-correlation distances $\delta_f(\lambda)$. The equations indicate a trend of decreasing fringe contrast with increasing spectral spread of $\delta_f(\lambda)$ when the spacing D is enlarged. This is seen in the data in Fig. 2b. Due to the cyclic dependence of the ambiguity functions on the auto-correlation distances, the fringe contrast oscillates with the spacing D as seen in Fig. 2b. Since the auto-correlation distances depend on both the grating period differential f_1-f_2 and their spacing, there are a continuous range of conditions for significant moiré effects. In the example of Fig. 2 a small gap between two gratings of the same period produces the effect. Alternatively if two gratings are overlaid with no spacing, a proper difference in periods also maximizes the moiré fringes. The fringe period scales linearly with the G_2-to-image distance and inversely with the grating period. An extreme case is when G_2 is an amplitude grating which produces a moiré pattern at δ_2=0. It describes the classic moiré effect appearing immediately behind G_2. With a finite-sized source the fringe amplitude is the integral of Eq. 12 over the source distribution. For a significant moiré effect the source size S should be less than half the source period P_s. Equivalently, the lateral coherence of the source at the first grating, $\lambda L_1/S$, should be greater than $2\delta_1 P_1$. The extreme is when G_1 is an amplitude grating, which produces a moiré effect at δ_1=0. In this case there is no limit on the source size since G_1 filters the source into a set of line sources.

Modeling of the three-grating system

Here the first two gratings are widely separated (Fig. 3a). Previous equations for the two-grating system describe the wave front before the 3rd grating. Consider the phase difference between the A_mB_1 and $A_{m+1}B_{-1}$ terms of the wave amplitude (Eq. 4–6). It is wavelength independent and invariant with the diffraction order m at a specific "echo" plane at a distance L_2 downstream from the G_2 grating, where

$$L_2 = D_1[f_1/(2f_2-f_1)]. \quad (19)$$

At the echo plane the wave amplitude contains the sum of pairs as

$$V_E(y) \propto \exp(ikL\cos^3\theta)\sum_m e^{i[\phi_0(m,1)+\phi_1(m,1)]}[A_m B_1 + A_{m+1}B_{-1}e^{i2\pi(f_1-2f_2)y}]. \quad (20)$$

Each pair represents an achromatic interference pattern superimposed onto a spherical wave, or a Fourier image[20] from G_1. For a polychromatic source the pairs are mutually incoherent due to the strong wavelength dependence of $\phi_1(m,1)$ (Eq. 6). When a third grating G_3 is placed on or near the echo plane and its frequency f_3 is near $2f_2-f_1$, each Fourier image forms a moiré pattern with G_3 at the image plane further downstream. The incoherent sum of these moiré patterns is the overall moiré pattern. Referring to Fig. 3a for geometric parameters, the normalized moiré fringe amplitude is given by

$$\frac{H_1(\lambda)}{H_0} = \frac{\chi_1(\delta_1 P_1, f_1)}{<T_1 T_1^*>} B_1 B_{-1}^* \frac{\chi_3(\delta_3 P_3, f_3)}{<T_3 T_3^*>}, \quad (21)$$

where the fractional auto-correlation distances are

$$\delta_1(\lambda) = \lambda \frac{f_1 L_1}{L\cos^3\theta}[(f_1-f_2)(L-L_1)+(f_3-f_2)L_3 - f_2(D_3-D_1)], \text{and} \quad (22)$$

$$\delta_3(\lambda) = \lambda \frac{f_3 L_3}{L\cos^3\theta}[(f_3-f_2)(L-L_3)+(f_1-f_2)L_1 - f_2(D_1-D_3)]. \quad (23)$$

Similar to the two-grating case, the moiré fringe period and the source period are both wavelength-independent:

$$P_d = L/[(f_3-f_2)(L-L_3)+(f_1-f_2)L_1 - f_2(D_1-D_3)], \text{and} \quad (24)$$

$$P_s = L/[(f_1-f_2)(L-L_1)+(f_3-f_2)L_3 - f_2(D_3-D_1)]. \quad (25)$$

The physical effects described by these results are similar to the two-grating case. With a polychromatic source the moiré effect is maximized for a specific set of auto-correlation distances $\delta_j(\lambda)$ which can be adjusted by the position of the third grating G_3, as seen in Fig. 4b; tilting the G_1 and G_3 gratings out of plane alters their transmission profiles, which changes the moiré fringe amplitude in a predictable way as shown in Fig. 4c and 4d; the moiré fringe period scales linearly with the G_3-to-image distance and inversely with the grating periods; the extreme case of significant moiré fringes at $\delta_3=0$ when G_3 is an amplitude grating describes the classic moiré effect which appears immediately behind G_3;

the source size should be less than half the source period P_s, or equivalently the lateral coherence of the source at the first grating, $\lambda L_1/S$, should be greater than $2\delta_1 P_1$; the extreme case of a moiré pattern at $\delta_1=0$ when G_1 is an amplitude grating describes the source being filtered by G_1 into a set of line sources.

Supplementary Material

Refer to Web version on PubMed Central for supplementary material.

Acknowledgments

We are grateful to Mr. Gary Melvin and Dr. Dumitru Mazilu for mechanical design and machining, to Dr. Mark Rivers, Department of Geophysical Sciences and Center for Advanced Radiation Sources, University of Chicago, for his help with the instrument control software. We thank Mr. Richard Kasica and Dr. Liya Yu of the Center for Nanoscale Science and Technology, National Institute of Standards and Technology for their assistance with fabrication.

References

1. Bonse U, Hart M. An X-Ray Interferometer. Appl Phys lett. 1965; 6:155–156.
2. Clauser JF, Li SF. Talbot-Von Lau Atom Interferometry with Cold Slow Potassium. Phys Rev A. 1994; 49:R2213–R2216. [PubMed: 9910609]
3. Momose A, Takeda T, Itai Y, Hirano K. Phase-contrast X-ray computed tomography for observing biological soft tissues. Nature Med. 1996; 2:473–475. [PubMed: 8597962]
4. Cloetens P, Guigay JP, DeMartino C, Baruchel J, Schlenker M. Fractional Talbot imaging of phase gratings with hard X-rays. Opt Lett. 1997; 22:1059–1061. [PubMed: 18185750]
5. Clauser, JF. Ultrahigh resolution interferometric x-ray imaging. US Patent No. 5,812,629. Sep 22. 1998
6. David C, Nohammer B, Solak HH, Ziegler E. Differential x-ray phase contrast imaging using a shearing interferometer. Appl Phys lett. 2002; 81:3287–3289.
7. Momose A, et al. Demonstration of X-Ray Talbot interferometry. Jpn J Appl Phys 2. 2003; 42:L866–L868.
8. Weitkamp T, et al. X-ray phase imaging with a grating interferometer. Opt Express. 2005; 13:6296–6304. [PubMed: 19498642]
9. Pfeiffer F, Weitkamp T, Bunk O, David C. Phase retrieval and differential phase-contrast imaging with low-brilliance X-ray sources. Nat Phys. 2006; 2:258–261.
10. Pfeiffer F, et al. Hard-X-ray dark-field imaging using a grating interferometer. Nat Mater. 2008; 7:134–137. [PubMed: 18204454]
11. Reid GT. Moire Fringes in Metrology. Optics and Lasers in Engineering. 1984; 5:63–93.
12. Gustafsson MGL. Surpassing the lateral resolution limit by a factor of two using structured illumination microscopy. J Microsc -Oxford. 2000; 198:82–87.
13. Zhou S, et al. Fourier-based analysis of moire fringe patterns of superposed gratings in alignment of nanolithography. Opt Express. 2008; 16:7869–7880. [PubMed: 18545497]
14. Cowley JM, Moodie AF. Fourier Images. 4 the Phase Grating. Proceedings of the Physical Society of London. 1960; 76:378–384.
15. Miao H, et al. Enhancing Tabletop X-Ray Phase Contrast Imaging with Nano-Fabrication. Scientific Reports. 2015; 5:13581. [PubMed: 26315891]
16. Miao H, Gomella AA, Chedid N, Chen L, Wen H. Fabrication of 200 nm Period Hard X-ray Phase Gratings. Nano Lett. 2014; 14:3453–3458. [PubMed: 24845537]
17. Bruning JH, et al. Digital wavefront measuring interferometer for testing optical surfaces and lenses. Appl Opt. 1974; 13:2693–2703. [PubMed: 20134757]
18. Panna A, et al. Performance of low-cost X-ray area detectors with consumer digital cameras. Journal of Instrumentation. 2015; 10:T05005.

19. Yashiro W, Momose A. Effects of unresolvable edges in grating-based X-ray differential phase imaging. Opt Express. 2015; 23:9233–9251. [PubMed: 25968757]

20. Cowley JM, Moodie AF. Fourier Images. 1 the Point Source. Proceedings of the Physical Society of London Section B. 1957; 70:486–496.

21. Hussey DS, Pushin DA, Huber MG, Jacobson DL. manuscript in preparation.

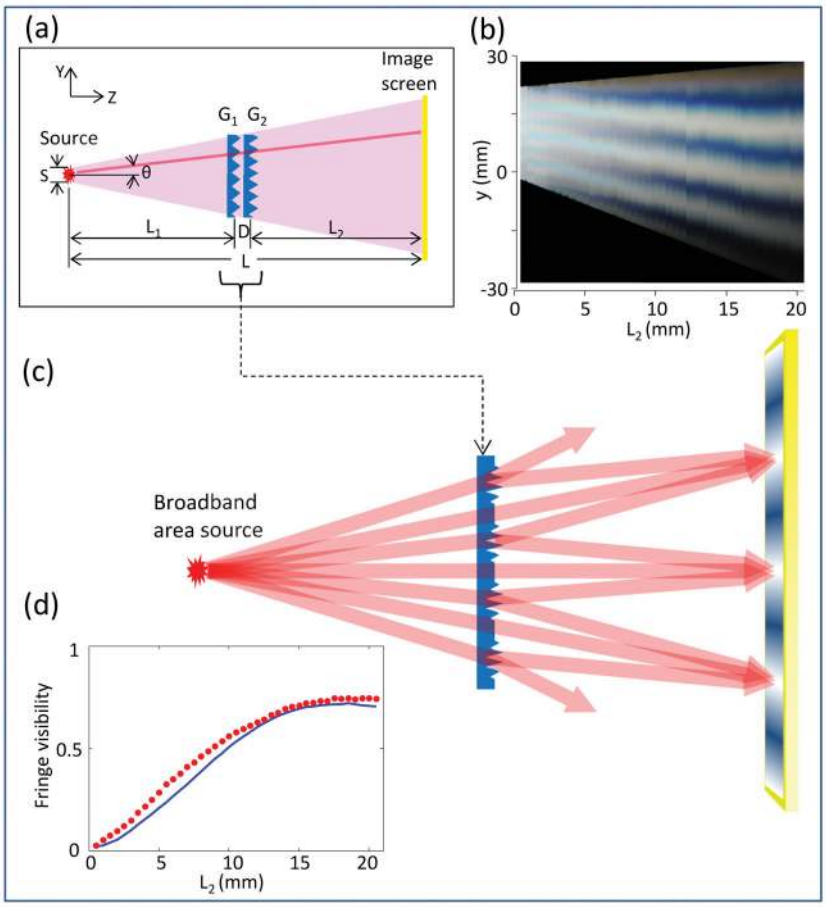

Figure 1.

An example of the phase moiré effect between two transparent phase gratings, (**a**) A white light source of a finite size illuminates the gratings. A frosted-glass screen captures the projected color image. (**b**) The vertical cross-section of the image as a function of the grating-to-screen distance L_2 shows a moiré pattern arising at a distance. Supplementary Fig. S1 includes a photo of the experimental setup and Supplemental video 1 shows the full images. (**c**) The explanation is that the two gratings act as a single phase grating whose phase oscillation is modulated by a beat pattern, representing interleaved strongly and weakly diffracting areas. Photons transmitting through the strongly diffracting areas are diffracted away from the direction of straight radial projection, giving rise to intensity bands at a distant plane. (**d**) Dependence of measured (red dots) and theoretically calculated (blue line) fringe visibility on the distance L_2. Measurement uncertainty was 0.003.

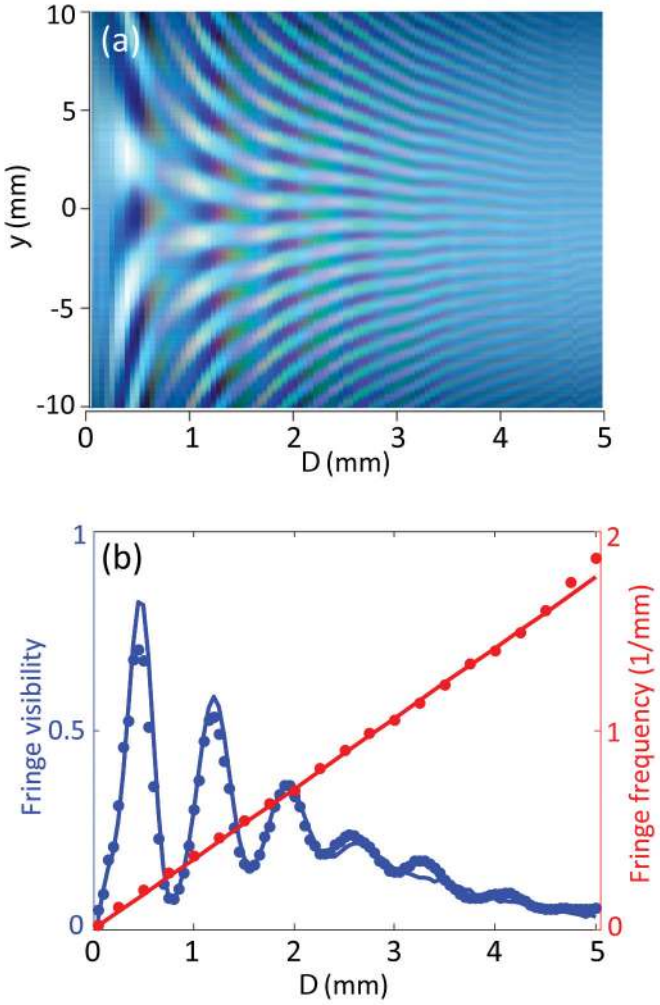

Figure 2.

Dependence of the moiré pattern on the inter-grating spacing in the setup in Fig. 1. (**a**) In the moiré carpet, the fringe pattern at a given inter-grating spacing D is shown as a vertical strip. The strips for the range of D values are stitched into the carpet. (**b**) Quantitative comparison of the moiré fringe visibility (blue) and spatial frequency (red) between theoretical calculations (solid lines) and experimental results (dots), as functions of the spacing D. Measurement uncertainty of fringe visibility was 0.003, of fringe frequency was 0.05 mm^{-1}.

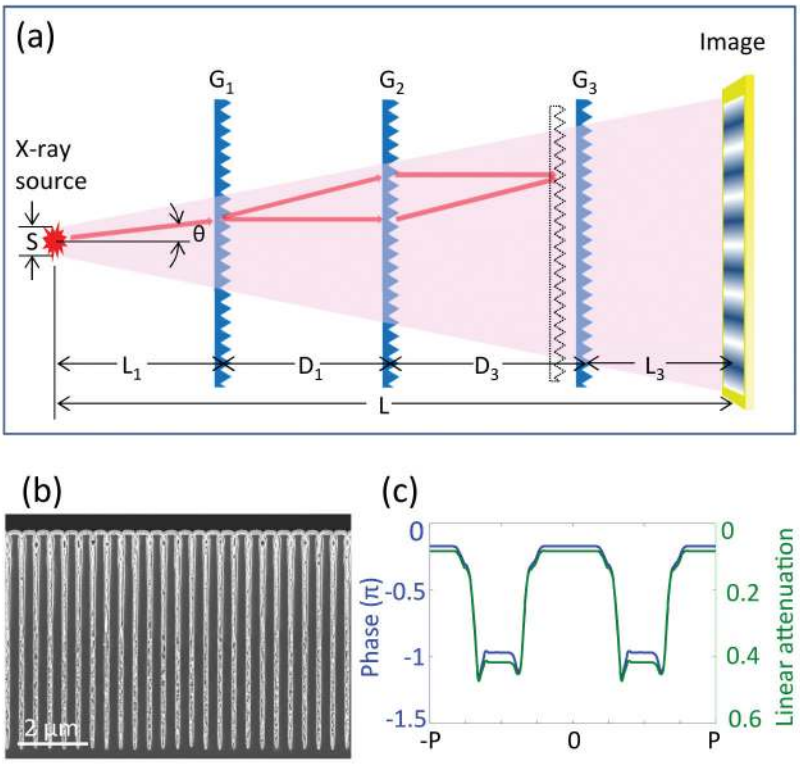

Figure 3.

The moiré effect among three phase gratings underlies a polychromatic far-field interferometer in this x-ray example. (**a**) Under a cone beam the first two gratings form a series of achromatic interference patterns at a plane downstream. The third grating is positioned on or near the plane to form moiré fringes at a distance. (**b**) SEM image of a cross section of the phase grating G_1. Trenches in silicon are filled with gold to cause a periodic profile of phase shift. (**c**) The grating SEM cross sections were used to calculate their phase shift and linear attenuation profiles. Data of the G_1 grating at 27.5 keV are shown. The sharp dips are produced by a thin layer of Pt.

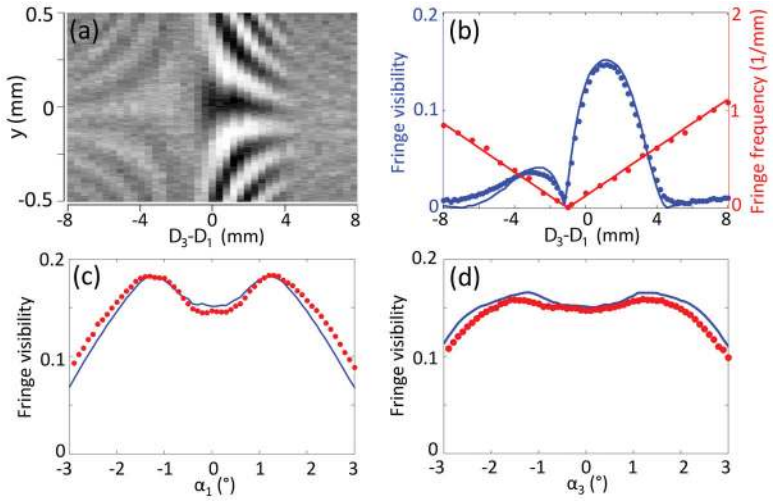

Figure 4.

Experimental data from the x-ray polychromatic far-field interferometer with mismatched grating periods. (**a**) The moiré carpet shows the evolution of the fringe pattern as the longitudinal position of the third grating is scanned. (**b**) Quantitative comparison of the fringe visibility (blue) and spatial frequency (red) between theoretical calculations (solid lines) and measurements (dots), as functions of the position of the G_3 grating. Measurement uncertainty of fringe visibility was 0.005, of fringe frequency was 0.05 mm^{-1}. (**c**) Theoretical (solid blue line) and measured (red dots) fringe visibilities as a function of the out-of-plane tilt of the grating G_1. (**d**) The same comparison for the G_3 grating. The peak fringe visibility of 19.4% was reached by optimizing both position and tilts.

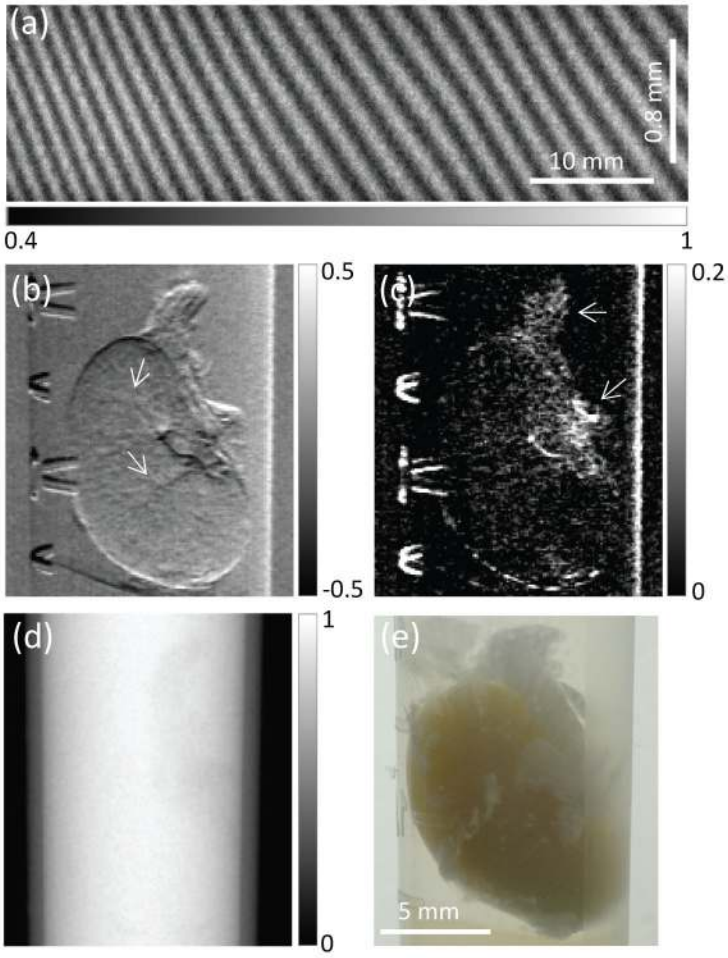

Figure 5.

Multi-modal x-ray projection images of a mouse kidney specimen immersed in water. (**a**) A single shot image of the grating area without the specimen shows the moiré fringes. Gray scale is the normalized image intensity. (**b**) The differential phase image reveals the outline and internal blood vessels (white arrows) of the kidney, together with the graduation marks on the centrifuge tube. Gray scale is in radians. (**c**) The de-coherence image shows reduced moiré fringe amplitude in fatty tissue (white arrows) and at the edges of the graduation marks. Gray scale is the linear attenuation coefficient. (**d**) Conventional attenuation-contrast radiography shows the fatty tissue as darker areas indicating lower density. Gray scale is the linear attenuation coefficient. (e) A photograph of the kidney specimen suspended in water in the centrifuge tube.